

Title: Deep Learning Predicts Mammographic Breast Density in Clinical Breast Ultrasound Images
Arianna Bunnell, MS.

Affiliations: Information and Computer Sciences, University of Hawai'i at Mānoa, Honolulu, HI, USA.
University of Hawai'i Cancer Center, Honolulu, HI, USA.

Address: POST Bldg Room 305B; 1680 East-West Rd; Honolulu, HI 96822

Thomas Wolfgruber, PhD.

Affiliations: University of Hawai'i Cancer Center, Honolulu, HI, USA

Address: University of Hawaii Cancer Center; 701 Ilalo St; Suite 522; Honolulu, HI 96813, USA.

Brandon Quon

Affiliations: University of Hawai'i Cancer Center, Honolulu, HI, USA

Address: University of Hawaii Cancer Center; 701 Ilalo St; Suite 522; Honolulu, HI 96813, USA.

Kailee Hung, BS.

Affiliation: Information and Computer Sciences, University of Hawai'i at Mānoa, Honolulu, HI, USA.

Address: POST Bldg Room 306C; 1680 East-West Rd; Honolulu, HI 96822

Brenda Hernandez, PhD, MPH.

Affiliations: University of Hawai'i Cancer Center, Honolulu, HI, USA

Address: University of Hawaii Cancer Center; 701 Ilalo St; Suite 522; Honolulu, HI 96813, USA.

Peter Sadowski, PhD.

Affiliation: Information and Computer Sciences, University of Hawai'i at Mānoa, Honolulu, HI, USA.

Address: POST Bldg Room 306C; 1680 East-West Rd; Honolulu, HI 96822

Corresponding Author: John A Shepherd, PhD.

Affiliation: University of Hawai'i Cancer Center, Honolulu, Hawaii, USA.

Address: University of Hawaii Cancer Center; 701 Ilalo St; Suite 522; Honolulu, HI 96813, USA.

ABSTRACT

Background. Mammographic breast density, as defined by the American College of Radiology's Breast Imaging Reporting & Data System (BI-RADS), is one of the strongest risk factors for breast cancer, but is derived from mammographic images, limiting the utility of risk evaluation to women participating in screening mammography. Breast ultrasound (BUS) is an alternative breast cancer screening modality, particularly useful for early detection in low-resource, rural contexts with no access to mammography. To date, BUS has not been used to inform risk models that need breast density. We asked if BUS can accurately quantify breast density calibrated to mammography density for use directly in risk models. The purpose of this study was to explore an artificial intelligence (AI) model to predict BI-RADS mammographic breast density category from clinical, handheld BUS imaging.

Methods. All data are sourced from the Hawai‘i and Pacific Islands Mammography Registry, which collects breast health information and imaging from all women undergoing screening or diagnostic breast imaging (2009-onwards) at three clinical partner sites. We compared deep learning methods for predicting mammographic breast density directly from BUS imaging, as well as machine learning models trained to make predictions from image statistics alone. The use of AI-derived BUS breast density as a risk factor for breast cancer was then compared to clinical BI-RADS breast density while adjusting for age. The BUS data were split by individual into 70/20/10% groups for training, validation for hyperparameter tuning, and held-out testing for reporting results.

Results. 405,120 clinical BUS images from 14,066 women were selected for inclusion in this study, resulting in 9,846 women for training (302,574 images), 2,813 for validation (11,223 images), and 1,406 testing (4,042 images). On the held-out testing set, the strongest AI model achieves AUROC 0.854 predicting BI-RADS mammographic breast density from BUS imaging and outperforms all shallow machine learning methods based on image statistics. In cancer risk prediction, age-adjusted AI BUS breast density predicted 5-year breast cancer risk with 0.633 AUROC, as compared to 0.637 AUROC from age-adjusted clinical breast density.

Conclusions. BI-RADS mammographic breast density can be estimated from BUS imaging with high accuracy using a deep learning model. The AI model provided superior estimates to other machine learning approaches. Furthermore, we demonstrate that AI-derived BUS breast density is predictive of 5-year breast cancer risk in our population.

KEYWORDS

INTRODUCTION

Other than age, mammographic breast density is one of the strongest risk factors for breast cancer. Breast density has been extensively studied over the past 30 years and is included in many breast cancer risk models (3-5). A recent meta-analysis showed that having extremely dense breasts increased lifetime breast cancer risk by 2.11 times over women with scattered dense breast tissue (BI-RADS density B), even when adjusted for BMI and age (6). Furthermore, high breast density lowers the sensitivity of mammography leading to a federal mandate to report breast density to all women undergoing screening mammography (7). Thus, many women have direct knowledge of the breast density and can apply it to readily available risk models. Women at high risk of developing breast cancer have multiple options for lowering their risk including lifestyle choices (8), and chemoprevention (9-11). However, there are many parts of the world that are either too resource-limited or too remote to have access to screening mammography programs. Without mammography, clinical breast density has not been available for comprehensive breast cancer risk assessment.

Breast ultrasound (BUS) is a sensitive method for detecting breast cancer and is broadly used around the world as primary screening in lower resource settings (12-14), secondary screening for women with dense breast tissue (15-17), and follow-up adjuvant imaging (18, 19). However, mammography is preferred, when available, due to its lower false-positive rate (20). Ideally, breast density would be available from accessible breast imaging technologies, like BUS, with a calibration equivalent to mammographic density.

Image contrast in B-mode BUS is based on the boundaries where density changes. See **Figure 1** for examples of matched BUS and mammography images at different mammographic densities. These boundary features have been investigated in the past to derive density-like measures. Jud et al. (21) used linear regression of variable defined by the grey-level values normalized into 16 bins. Their model was able to estimate percent mammographic density with an accuracy of $R^2 = 0.67$ but suffered from calibration issues in external datasets (22).

In the past decade, there has been a revolution in machine learning and convolutional neural deep learning networks with substantial literature on predicting mammographic breast density from mammograms using artificial intelligence (AI) (23-25) and deriving breast cancer risk from mammograms directly (26-29). The purpose of this study is to explore the use of AI to estimate breast density from BUS images. We further explore

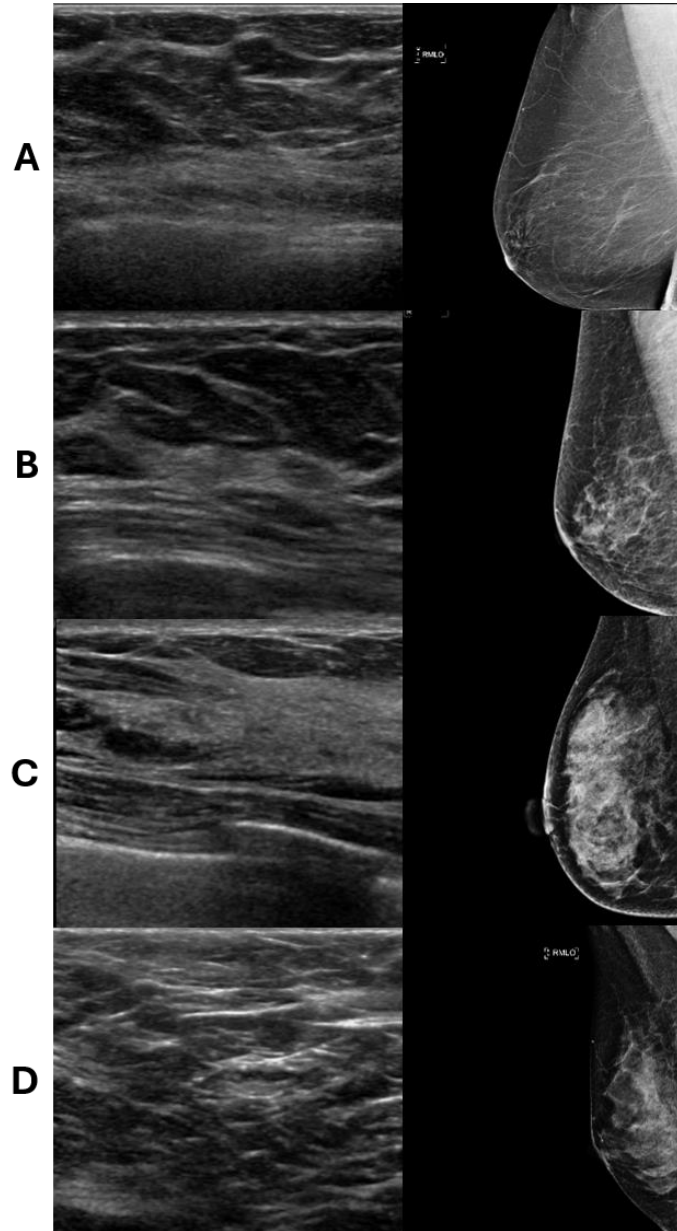


Figure 1. Example clinical breast ultrasound (left) and right mediolateral oblique digital 2D mammography (right) images, selected from the dataset included in this work. Image sets are labeled with their BI-RADS breast density category. Images have been cropped for ease of display.

the use of our AI-derived BUS breast density in place of mammographic density in a simple risk model.

METHODS

Using BUS images without cancer temporally linked to a mammogram visit and to future cancer outcomes, we constructed a deep learning model to predict BI-RADS mammographic density. We compared our deep learning model to a previously-derived machine learning method using grey-level image histograms. We then compare the predictive ability of clinical, AI-derived and image grey-level histogram-based BUS estimates of breast density in estimating 5-year breast cancer risk.

Study sample

All women included in this study participated in either screening or diagnostic BUS imaging in the Hawai‘i and Pacific Islands Mammography Registry (HIPIMR; see Supplement). Women were selected for inclusion if they met all the following criteria: (a) had at least one negative screening 2D mammography visit; (b) had a negative, benign, or probably benign BUS visit within one year of their mammograms; (c) had a clinical BI-RADS breast density; (d) had the standard four views captured at their screening mammogram; and (e) had no history of breast cancer prior to screening mammogram (See Supplement for complete inclusion/exclusion criteria). From these, cases were defined as women diagnosed with invasive breast cancer at least 6 months and no more than 5 years from their extracted BUS exam. Controls were selected from women who did not develop cancer. See **Figure 2** for the complete data flow diagram.

Imaging data preparation

Clinical BUS data are highly noisy data, with many artifacts such as Color Doppler blood flow highlighting, sonographer text annotations, and lesion caliper markers which can interfere with AI

model learning. We implement a cleaning pipeline developed in-house called BUSClean (30) to remove these artifacts and standardize BUS images converted from DICOM to PNG.

Data splitting

The development dataset was split by woman, stratified by clinical BI-RADS breast density category, with 80% assigned to the training data set and 20% assigned to the validation split for hyperparameter tuning and early stopping determination. The case-control matched testing set was reserved for performance evaluation. Each woman and her images are only present in a single data split. We duplicated the validation dataset to create *curated* and *uncurated* validation sets. In brief, the *curated* validation set has extensive preprocessing applied to remove clinical artifacts, while the *uncurated* validation set had only invalid scans removed and scans with multiple views split.

See Supplement for details.

Deep learning model

Three deep learning models were trained in PyTorch (31) using three distinct ImageNet-pretrained architectures: DenseNet121 (32), ViT-B/32 (33), and ResNet50 (34), selected to represent a diverse range of deep learning architecture designs. Hyperparameters for each were optimized over 25 trials using the TPESampler in Optuna (35). **Supplemental Table 1** displays the search space. The best-performing model and hyperparameters on the curated validation set was selected as the final architecture and retrained (see Supplement for training configuration). The final deep learning architecture was selected based on performance on the curated validation set.

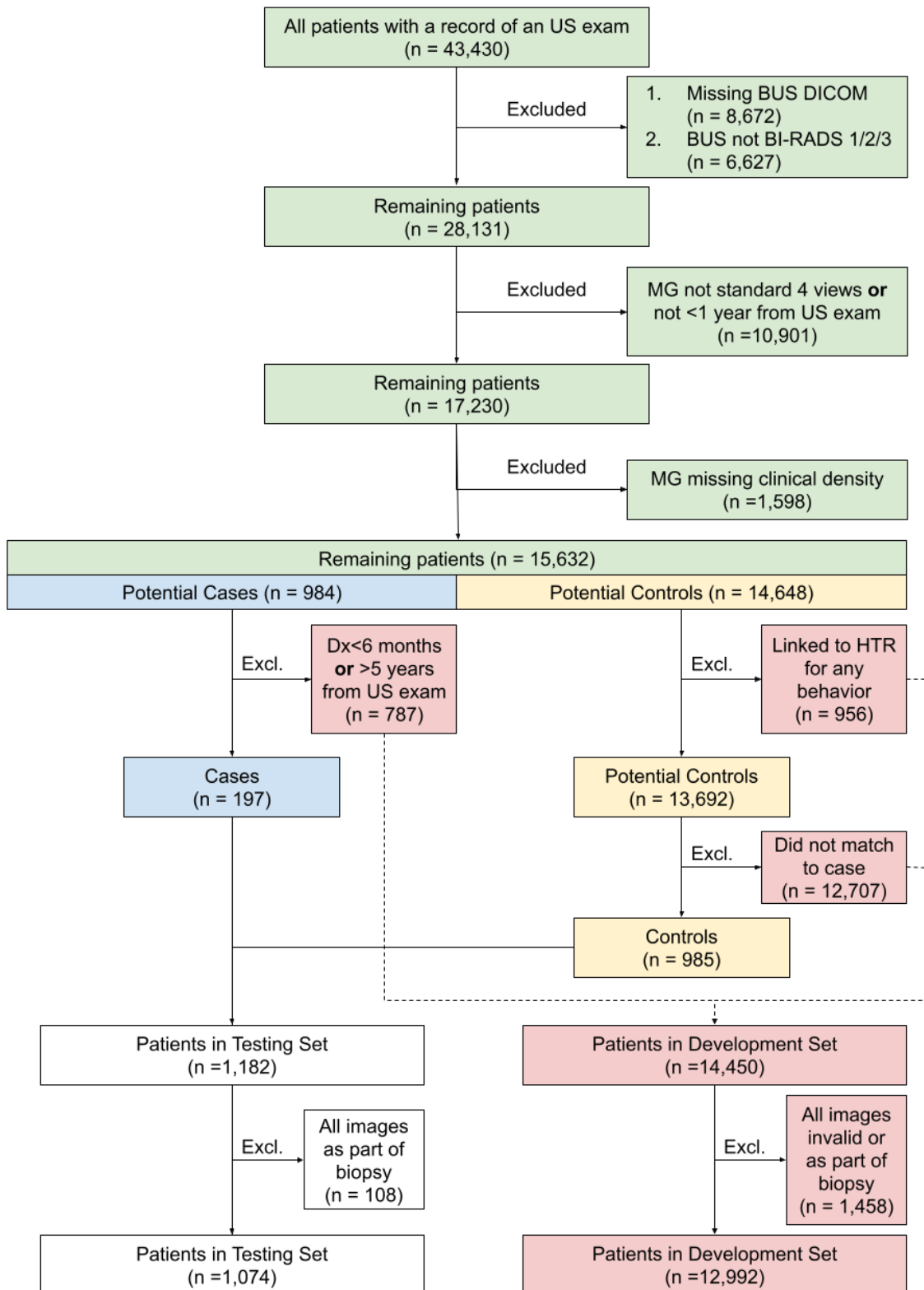


Figure 2. Flow diagram showing data selection process from the HIPIMR. Cases and controls were selected from the same pool of 15,632 patients with matched mammograms with density records and BUS exams. 197 cases and 965 controls, matched on birth year, were selected for the testing set. After exclusion of invalid images, 1,074 women remained. The remaining 12,992 eligible women with valid images were allocated to the development set. Dx = diagnosis; MG = mammogram; BUS = breast ultrasound; Excl. = excluded; HTR = Hawai‘i Tumor Registry.

Image histogram models

Prior work in estimating percentage mammographic breast density from B-mode BUS imaging from Jud et al. makes use of gray-level image histograms with equally-sized intervals in a linear regression model (21). We implement a version of their method adapted for the categorical BI-RADS breast density measure (see Supplement). Logistic regression, random forest, and multi-layer perceptron (MLP) models were constructed using the gray-level image histogram intervals as features to predict BI-RADS categorical breast density.

Statistical analysis

Statistical analysis was undertaken in two steps. The first step demonstrates AI model accuracy in predicting breast density category from BUS. The second step demonstrates utility of predicted BUS BI-RADS breast density category in breast cancer risk modelling. See Supplement for the implementation details of both steps. To assess AI model performance in predicting breast density from BUS, all models are evaluated by their micro-averaged AUROC over all density categories with 95% confidence intervals estimated using DeLong's method (1, 2) on the testing set. We use micro-averaged AUROC for increased stability under class imbalance. We present AUROC on the overall testing set as well by BUS machine manufacturer, binned patient age at BUS exam, cancer status, and BUS exam BI-RADS category. We additionally compute Kendall's τ -b (36) between clinical density and predicted density from BUS to compare agreement. As a comparator, we computed mammographic density using (23) on all included women and computed Kendall's τ -b between these predictions and clinical density. We use interpretation ranges from (37). To demonstrate utility in cancer risk prediction, we constructed logistic regression models of breast cancer risk from age at BUS exam and mammographic breast density. Effect of breast density

category and standardized age was compared via computation of odds ratios with 95% Wald confidence intervals.

RESULTS

Study sample characteristics

The characteristics of all 14,066 women (15,632 identified for inclusion from the HIPIMR) included in the study (mean age at BUS exam \pm standard deviation, 53 ± 12 years) are described

Table 1. Study sample characteristics. BUS = breast ultrasound; MG = mammogram; Dx = diagnosis; IQR = inter-quartile range; SD = standard deviation.

	Overall	Training Set	Curated Validation Set	Uncurated Validation Set	Testing Set
Women, N	14,066	10,393	2,593	2,599	1,074
Women with benign findings, N (%)	-	-	-	-	896 (83.4)
Women with malignant findings, N (%)	-	-	-	-	178 (16.6)
Mean age at US, years (SD)	53.4 (11.9)	53.4 (11.9)	53.3 (12.0)	53.3 (12.0)	53.8 (12.1)
Mean age at MG, years (SD)	53.4 (11.9)	53.4 (11.9)	53.2 (12.0)	53.3 (12.0)	53.8 (12.1)
Mean age at diagnosis, years (SD)	-	-	-	-	60.4 (11.4)
Women with fatty/A breasts, N (%)	478 (3.4)	344 (3.3)	99 (3.8)	99 (3.8)	35 (3.3)
Women with scattered/B breasts, N (%)	5,486 (39.0)	4,088 (39.3)	987 (38.1)	987 (38.1)	409 (38.1)
Women with heterogeneous/C breasts, N (%)	6,291 (44.7)	4,615 (44.4)	1,178 (45.4)	1,182 (45.5)	494 (45.9)
Women with dense/D breasts, N (%)	1,811 (12.9)	1,346 (13.0)	329 (12.7)	329 (12.6)	136 (12.7)
Menopausal women, N (%)	4,365 (31.0)	3,210 (30.9)	806 (31.1)	810 (31.2)	345 (32.1)
Premenopausal women, N (%)	480 (3.4)	347 (3.3)	83 (3.2)	84 (3.2)	49 (4.6)
Unknown menopausal status, N (%)	9,221 (65.6)	6,836 (65.8)	1,704 (65.7)	1,705 (65.6)	680 (63.3)
Median gap btw. MAM & US, days (IQR)	5.0 (20.0)	5.0 (20.0)	4.0 (19.0)	4.0 (19.0)	6.0 (19.8)
Median gap btw. MAM & Dx, days (IQR)	-	-	-	-	822.0 (816.8)
Median gap btw. US & Dx, days (IQR)	-	-	-	-	808.5 (808.5)
Images, N	405,120	302,574	69,842	73,930	28,616
Mean no. of images per woman, N (SD)	28.8 (22.9)	29.1 (23.1)	26.9 (21.8)	28.5 (22.5)	26.6 (21.9)
Images with benign findings, N (%)	-	-	-	-	23,901 (83.5)
Images with malignant findings, N (%)	-	-	-	-	4,715 (16.5)
US BI-RADS 1 images, N (%)	58,428 (14.4)	43,163 (14.3)	10,856 (15.5)	11,223 (15.2)	4,042 (14.1)
US BI-RADS 2 images, N (%)	238,268 (58.8)	177,280 (58.6)	41,313 (59.2)	43,569 (58.9)	17,419 (60.9)
US BI-RADS 3 images, N (%)	108,424 (26.8)	82,131 (27.1)	17,673 (25.3)	19,138 (25.9)	7,155 (25.0)
Images of fatty/A breasts, N (%)	11,525 (2.9)	8,416 (2.9)	2,223 (3.2)	2,346 (3.2)	886 (3.1)
Images of scattered/B breasts, N (%)	151,015 (37.6)	115,394 (38.1)	25,794 (36.9)	27,023 (36.5)	9,827 (34.3)
Images of heterogeneous/C breasts, N (%)	180,927 (45.1)	135,622 (44.8)	31,941 (45.7)	34,131 (46.2)	13,364 (46.7)
Images of dense/D breasts, N (%)	57,565 (14.4)	43,142 (14.2)	9,884 (14.2)	10,430 (14.1)	4,539 (15.9)
Images on PHILIPS System, N (%)	363,308 (89.7)	271,905 (89.9)	64,204 (91.9)	66,716 (90.2)	24,687 (86.3)
Images on ATL System, N (%)	25,297 (6.2)	17,877 (5.9)	3,723 (5.3)	4,212 (5.7)	3,208 (11.2)
Images on SIEMENS System, N (%)	12,617 (3.1)	9,795 (3.2)	1,495 (2.1)	2,379 (3.2)	443 (1.5)
Images on TOSHIBA System, N (%)	3,763 (0.9)	2,862 (0.9)	420 (0.6)	623 (0.8)	278 (1.0)
Images on GE System, N (%)	126 (0.0)	126 (0.0)	0 (0.0)	0 (0.0)	0 (0.0)
Images on ALOKA System, N (%)	9 (0.0)	9 (0.0)	0 (0.0)	0 (0.0)	0 (0.0)

in **Table 1**. See the Supplement for complete inclusion/exclusion criteria-specific counts. 405,120 total BUS images were included in this study

Deep learning model

Based on superior performance in the curated validation set, DenseNet121 was chosen as the final deep learning model architecture (see **Supplemental Table 1**). Performance with confidence interval estimates on the complete testing set, as well as subgroups of interest, are reported in Error! Reference source not found.. DenseNet121 identified patients with BI-RADS breast density category A, B, C, and D from all other categories with AUROC 0.84, 0.79, 0.72, and 0.88 respectively on the unseen test set. **Figure 3** displays receiver operating characteristic curves for the DenseNet121 on the unseen test set, separated by ground truth mammographic density category. In comparison of performance on subgroups (see **Supplemental Table 4**), non-

Table 2. Overall performance statistics for the DenseNet121, logistic regression, and random forest models. See **Supplemental Table 4** for subgroup performance.

		AUC* (95% C.I.)	by BI-RADS breast density category			
			Overall	Fatty/A	Scattered/B	Heterogen./C
DenseNet121	Per-image	0.840 (0.838, 0.842)	0.857 (0.847, 0.867)	0.761 (0.755, 0.766)	0.673 (0.667, 0.679)	0.839 (0.833, 0.846)
	Per-patient	0.854 (0.842, 0.866)	0.841 (0.790, 0.891)	0.787 (0.759, 0.815)	0.719 (0.689, 0.749)	0.879 (0.848, 0.910)
Logistic Reg	Per-image	0.771 (0.768, 0.774)	0.594 (0.574, 0.613)	0.607 (0.601, 0.614)	0.584 (0.577, 0.590)	0.583 (0.574, 0.592)
	Per-patient	0.795 (0.781, 0.809)	0.642 (0.552, 0.732)	0.654 (0.620, 0.687)	0.621 (0.588, 0.654)	0.668 (0.619, 0.716)
Random Forest	Per-image	0.759 (0.756, 0.762)	0.604 (0.586, 0.623)	0.597 (0.590, 0.604)	0.540 (0.533, 0.546)	0.625 (0.617, 0.634)
	Per-patient	0.794 (0.780, 0.808)	0.698 (0.620, 0.776)	0.639 (0.605, 0.673)	0.575 (0.541, 0.609)	0.727 (0.680, 0.774)

*AUC is a micro-averaged one vs. rest AUROC over all density categories, except for density subgroups. For density subgroups, one vs. rest AUC for each category is shown. 95% confidence intervals are calculated using DeLong's method (1, 2).

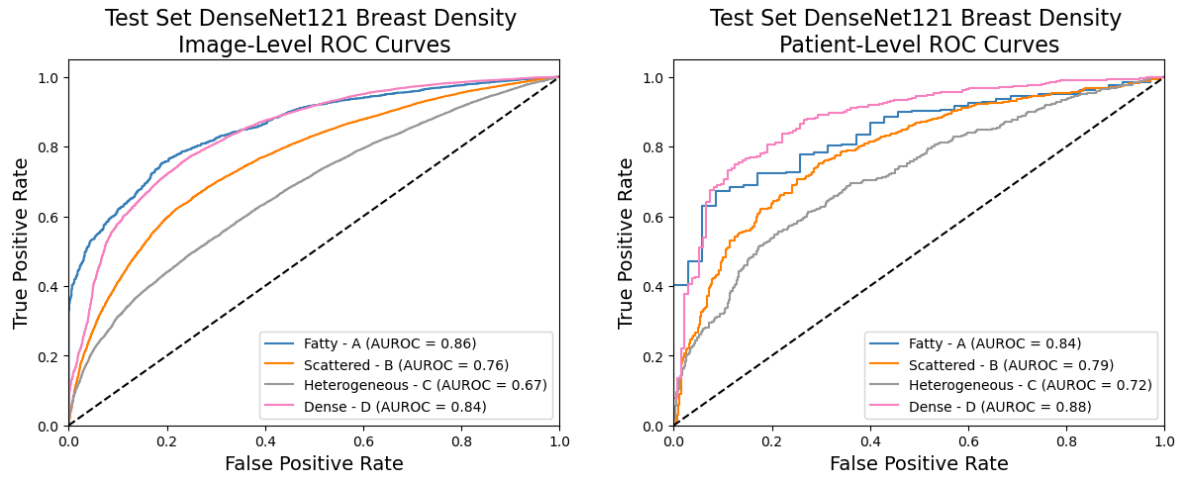


Figure 3. BUS AI model receiver operating characteristic (ROC) curves for the image-level predictions (left) and when aggregated through arithmetic averaging to patient-level (right).

overlapping confidence intervals were observed between patients imaged Toshiba machines and other BUS machine manufacturers, with higher performance in Toshiba machines and patients under 50 years old and over 65 years old, with higher performance in younger patients. Performance between all other subgroups was found to be non-significantly different. **Supplemental Figure 1** shows example saliency maps highlighting the areas of the BUS scans which may be of particular importance for the deep learning model's predictions on the unseen test set, computed using integrated gradients (38, 39).

Image histogram models

Performance results for the baseline random forest and logistic regression models (see **Supplemental Table 2** for model selection and tuning details) are presented in Error! Reference source not found.. Logistic regression from the gray-level image histograms identified patients in the held-out testing set with BI-RADS breast density A, B, C, and D from all other categories with AUROC 0.642, 0.654, 0.621, and 0.668, respectively. The image histogram random forest model identified patients in the held-out testing set with BI-RADS breast density A, B, C, and D from all other categories with AUROC 0.698, 0.639, 0.575, and 0.727, respectively. 95% confidence

intervals for performance overlap between linear (logistic regression) and nonlinear (random forest) modelling from the gray-level image histograms in every BI-RADS breast density category.

Agreement to Clinical Density

Kendall's τ -b between predicted BUS density and clinical density was found to be 0.47 (moderate agreement). Predicted BUS density was calculated per-patient by taking an arithmetic mean over the predicted class with the largest probability from each image and rounding to the nearest integer. Kendall's τ -b between mammographic density from (23) and clinical density was found to be 0.60 (moderate agreement). Predicted mammographic density from (23) was defined as the predicted class with the largest probability.

Cancer Risk Modeling

The benchmark for age-adjusted AI-derived BI-RADS breast density performance was performance of age-adjusted clinical BI-RADS breast density scores, assigned by the examining radiologist at the time of each woman's matched mammogram. We additionally computed the predictive power of age alone. The age-adjusted, clinical, BI-RADS breast density category predicted cancer occurrence with 0.637 AUROC (95% confidence interval (0.594, 0.679)). The BUS AI density model BI-RADS category predicted cancer occurrence with AUROC 0.633 (0.590, 0.676). Standardized age alone predicted cancer occurrence with AUROC 0.628 (0.585, 0.671). Odds ratios (ORs) for the individual explanatory variables are presented in **Supplemental**

Table 3. The ORs with 95% confidence intervals for the extremely dense/D (class B/scattered as reference) clinical and BUS AI density were 1.54 (1.31, 1.81) and 1.50 (1.28, 1.76), respectively.

Additional experiments modeling cancer risk from clinical mammographic breast density in an age-matched cohort resulted in an AUROC of 0.546 (0.478, 0.614), supporting the observed result

in the non-age-matched cohort that clinical breast density did not provide additional predictive power. Cases in the age-matched cohort were the same cases included in the previously-defined testing set. Controls were re-matched and selected from the previously-defined validation and testing set. BUS density was not computed for this group.

DISCUSSION

We found that BI-RADS breast density can be estimated through machine learning methods from BUS images and that our deep learning model outperformed other approaches. We also found that that the top performing BUS breast density estimate had comparable performance or at least was not inferior to clinical BI-RADS breast density for predicting 5-year breast cancer risk in an unseen test set. Furthermore, agreement to clinical density is shown to be similar to an open-source method for predicting density from the mammogram directly (23). We found that the deep learning model had similar performance in subgroups of BUS machine make and model, patient age, cancer status, diagnostic BI-RADS status. Given this robustness, breast density derived from our deep learning model should be broadly applicable to clinical situations globally, particularly in remote- and low-resource areas.

Limited prior work has investigated the prediction of mammographic breast density from ultrasound. Tissue speed-of-sound (SoS) using a dedicated non-diagnostic probe has been proposed for measuring mammographic breast density (40). It was found that non-dense (BI-RADS classes A & B) could be predicted from dense (BI-RADS C & D) breasts with AUROC = 0.887. However, the application of a dedicated BUS device for breast density has limited clinical applications or benefit over being able to get BUS from a clinical hand-held system. Our method can identify patients with extremely dense breasts (class D) with similar performance of AUROC

0.879. When dichotomized, our method identified dense (BI-RADS C & D) from non-dense (BI-RADS A & B) women with AUROC 0.823 (0.797, 0.848). Mammographic percent density has also been measured using SoS on a SoftVue (Delphinus Medical Technologies; MI, USA) ultrasound tomosynthesis system with an accuracy of $R^2 = 0.96$ (41-43). Ultrasound tomosynthesis systems are highly specialized equipment with high installation and maintenance costs which may not be appropriate for low-resource and rural areas. Handheld BUS is most directly applicable to rural and resource-limited scenarios due to portability and low cost. Additional non-mammographic methods of measuring breast density have also been explored, including microwave breast imaging (44), dual X-ray absorptiometry (45, 46), optical spectroscopy (46), and bioimpedance (47, 48). These methods, no matter their performance, are less desirable than integrating breast density into clinical BUS since they do not provide cancer detection in addition to density assessment the way clinical BUS does. If used in breast cancer screening, these alternative methods would need to be coupled with BUS or mammography to provide both detection and risk assessment.

Alternative BUS imaging-based biomarkers of breast cancer risk have been explored other than breast density. Breast parenchymal pattern from ultrasound measures the distribution of fat and ductal tissue in the breast. It can be classified by a breast radiologist into four categories: ductal, heterogeneous, mixed, and fibrous and has been found to be associated with breast cancer risk in the Chinese population (49, 50). Another biomarker of breast cancer risk identified from breast ultrasound imaging is glandular tissue component. Glandular tissue component is also a four-category classification which measures the degree of lobular involution observed in *screening* BUS (51). High glandular tissue component is associated with increased risk of breast cancer in women with extremely dense (BI-RADS D) breasts (51, 52). It may be that these measures have

complementary risk information to breast density but this has yet to be explored. We pursued breast density since it may be integrated into existing breast cancer risk models such as the BCSC, Tyer-Cuzick and others. Background echotexture, as defined by the ACR, is a three-category classification which has been found to be associated with both mammographic density and parity, known risk factors for breast cancer (53). AI combined with automated breast ultrasound (ABUS) performed with AUROC 0.979 for identifying background echotexture categories (54), however ABUS may be prohibitively costly for remote and low-resource rural areas.

The performance of the derived breast risk model using age alone was not significantly different from models with *either* clinical or BUS-derived density, limiting the insights we can draw about the added value of our measure in clinical breast cancer risk models. The typical effect has been found to be 2.1 to 2.3 times the relative risk for women with extremely dense (BI-RADS D) breasts over women with scattered density (BI-RADS B) (55, 56). The lack of observed effect of BI-RADS breast density in our study may be attributed to the imaging being from diagnostic visits. BUS is not a primary screening modality in Hawai‘i, and all exams included in this study are diagnostic exams requested after an initial mammogram. The characteristics of the diagnostic BUS population are likely different than a screening mammography population, on which most breast cancer risk evaluation is based. Future validation is needed in a population screened with BUS to verify our findings and confirm clinical utility of BUS-derived breast density in traditional breast cancer risk models.

Although our findings are promising, there are limitations to consider. First, there were relatively few women present in the lowest density category A (4%). This imbalance may be due to the ethnic breakdown of the population of the HIPIMR, with an estimated 60% of women in Hawai‘i identifying as Asian (alone or in combination with another race) in 2023 (57). Asian women have

been found to have denser breasts than women of other races (58, 59). Future work will explore sample enrichment with category A women. Another limitation of this work is that our risk model only consisted of age and breast density. Inclusion of other breast cancer risk factors may provide a more comprehensive assessment and validation of our method.

We conclude that estimation of categorical, BI-RADS breast density is possible from BUS imaging with acceptable accuracy for use in breast cancer risk assessment models. In cancer risk models, the performance of our measure of breast density indicates an association to cancer risk on par with clinical density in our dataset.

EVIDENCE BEFORE THIS STUDY

Age-adjusted mammographic breast density is one of the strongest risk factors for breast cancer and several artificial intelligence (AI) approaches exist for automatic breast density estimation from digital mammography imaging. When using breast ultrasound for primary screening, such as in low-resource medical contexts, breast density is not available. Lack of mammographic breast density limits the breast cancer risk evaluation which can be done. Prior work has shown that breast density can be estimated from modalities other than mammography, with varying levels of success. In ultrasound, speed-of-sound using specialized hardware or methods using automated/3D ultrasound have been the most successful. These methods have limited applicability in low-resource contexts (for ABUS) or require specialized hardware (speed of sound).

ADDED VALUE OF THIS STUDY

Our study proposes an AI method for estimation of BI-RADS mammographic breast density category from handheld breast ultrasound imaging and demonstrates the efficacy of breast density estimation from ultrasound in cancer risk assessment. This method could be used to provide more

complete breast cancer risk evaluation in rural and low-resource areas where mammography is not available, or in any context where women are primarily being screened with breast ultrasound.

IMPLICATIONS OF ALL THE AVAILABLE EVIDENCE

Breast ultrasound imaging contains information about mammographic breast density. Our study shows that BI-RADS mammographic breast density can be accurately estimated from clinical breast ultrasound data using artificial intelligence. Estimated breast density may be useful in performing breast cancer risk assessment in rural and low-resource areas, where mammography may not be available.

LIST OF ABBREVIATIONS

BUS = breast ultrasound

AUROC = area under the receiver operating characteristic curve

AI = artificial intelligence

BI-RADS = breast imaging-reporting and data system

ABUS = automated breast ultrasound

HIPIMR = Hawai‘i and Pacific Islands Mammography Registry

DECLARATIONS

Ethics approval and consent to participate. This study was approved by the WCG IRB (Study Number 1264170).

Consent for publication. Not applicable.

Availability of data and materials. The data that support the findings of this study are available from the Hawai‘i and Pacific Islands Mammography Registry (HIPIMR), but restrictions apply to the availability of these data. Data can be requested for research use through the HIPIMR’s website at hipimr.shepherdresearchlab.org. All code for running the trained models, creating the gray-level comparator method, and evaluation is available at <https://github.com/hawaii-ai/bus-density>.

Competing interests. The authors declare no conflicts of interest or financial interest.

Funding. This study was funded by NCI Grant 5R01CA263491-02.

Author’s Contributions. Arianna Bunnell: Methodology, Software, Investigation, Formal analysis, Writing - Original Draft, Visualization; Thomas Wolfgruber: Data Curation, Resources, Software; Brandon Quon: Data Curation, Resources; Kailee Hung: Software; Brenda Hernandez: Data Curation, Resources; Peter Sadowski: Conceptualization, Writing - Review & Editing, Supervision; John A. Shepherd: Conceptualization, Writing - Review & Editing, Supervision, Funding acquisition.

Acknowledgements.

REFERENCES

1. Jacob G. A python library for confidence intervals. 2023.
2. Sun X, Xu W. Fast implementation of DeLong’s algorithm for comparing the areas under correlated receiver operating characteristic curves. *IEEE Signal Processing Letters*. 2014;21(11):1389-93.
3. Tyrer J, Duffy SW, Cuzick J. A breast cancer prediction model incorporating familial and personal risk factors. *Statistics in medicine*. 2004;23(7):1111-30.
4. Gail MH, Brinton LA, Byar DP, Corle DK, Green SB, Schairer C, Mulvihill JJ. Projecting individualized probabilities of developing breast cancer for white females who are being examined annually. *JNCI: Journal of the National Cancer Institute*. 1989;81(24):1879-86.
5. Tice JA, Cummings SR, Smith-Bindman R, Ichikawa L, Barlow WE, Kerlikowske K. Using clinical factors and mammographic breast density to estimate breast cancer risk: development and validation of a new predictive model. *Annals of internal medicine*. 2008;148(5):337-47.
6. Bodewes F, Van Asselt A, Dorrius M, Greuter M, De Bock G. Mammographic breast density and the risk of breast cancer: a systematic review and meta-analysis. *The Breast*. 2022;66:62-8.

7. Berg WA, Seitzman RL, Pushkin J. Implementing the national dense breast reporting standard, expanding supplemental screening using current guidelines, and the proposed Find It Early Act. *Journal of Breast Imaging*. 2023;5(6):712-23.
8. Maramara T, Matos MC, Ardila S, Phantana-angkool A, Henry D. Minimizing Breast Cancer Risk with Diet and Exercise. *Current Breast Cancer Reports*. 2024;16(1):45-52.
9. Zaluzec EK, Sempere LF. Systemic and local strategies for primary prevention of breast cancer. *Cancers*. 2024;16(2):248.
10. Cuzick J, Chu K, Keevil B, Brentnall AR, Howell A, Zdenkowski N, Bonanni B, Loibl S, Holli K, Evans DG. Effect of baseline oestradiol serum concentration on the efficacy of anastrozole for preventing breast cancer in postmenopausal women at high risk: a case-control study of the IBIS-II prevention trial. *The Lancet Oncology*. 2024;25(1):108-16.
11. Yogendran L, Meis L, Burnside E, Schrager S. Management of women at high risk for breast cancer. *The Journal of the American Board of Family Medicine*. 2024;36(6):1029-32.
12. Yang L, Wang S, Zhang L, Sheng C, Song F, Wang P, Huang Y. Performance of ultrasonography screening for breast cancer: a systematic review and meta-analysis. *BMC Cancer*. 2020;20(1). doi: 10.1186/s12885-020-06992-1.
13. Sood R, Rositch AF, Shakoor D, Ambinder E, Pool K-L, Pollack E, Mollura DJ, Mullen LA, Harvey SC. Ultrasound for Breast Cancer Detection Globally: A Systematic Review and Meta-Analysis. *Journal of Global Oncology*. 2019(5):1-17. doi: 10.1200/jgo.19.00127.
14. He J, Chen W, Li N, Shen H, Li J, Wang Y, Tian J, Zhou B. China guideline for the screening and early detection of female breast cancer (2021, Beijing). *Zhonghua Zhong liu za zhi [Chinese Journal of Oncology]*. 2021;43(4):357-82.
15. Mainiero MB, Lourenco A, Mahoney MC, Newell MS, Bailey L, Barke LD, D'Orsi C, Harvey JA, Hayes MK, Huynh PT. ACR appropriateness criteria breast cancer screening. *Journal of the American College of Radiology*. 2016;13(11):R45-R9.
16. Urban LABD, Chala LF, Bauab SdP, Schaefer MB, Santos RPd, Maranhão NMdA, Kefalas AL, Kalaf JM, Ferreira CAP, Canella EdO. Breast cancer screening: updated recommendations of the Brazilian College of Radiology and diagnostic imaging, Brazilian breast disease society, and Brazilian federation of gynecological and obstetrical Associations. *Radiologia brasileira*. 2017;50:244-9.
17. Ren W, Chen M, Qiao Y, Zhao F. Global guidelines for breast cancer screening: a systematic review. *The Breast*. 2022;64:85-99.
18. Evans A, Trimboli RM, Athanasiou A, Balleyguier C, Baltzer PA, Bick U, Camps Herrero J, Claußer P, Colin C, Cornford E. Breast ultrasound: recommendations for information to women and referring physicians by the European Society of Breast Imaging. *Insights into imaging*. 2018;9:449-61.
19. Radiology ACo. ACR practice parameter for the performance of a diagnostic breast ultrasound examination. *American College of Radiology Website*. 2021.
20. Berg WA, Bandos AI, Mendelson EB, Lehrer D, Jong RA, Pisano ED. Ultrasound as the primary screening test for breast cancer: analysis from ACRIN 6666. *Journal of the National Cancer Institute*. 2016;108(4):djv367.
21. Jud SM, Häberle L, Fasching PA, Heusinger K, Hack C, Faschingbauer F, Uder M, Wittenberg T, Wagner F, Meier-Meitinger M, Schulz-Wendtland R, Beckmann MW, Adamietz BR. Correlates of mammographic density in B-mode ultrasound and real time elastography. *European Journal of Cancer Prevention*. 2012;21(4):343-9.
22. Behrens A, Fasching PA, Schwenke E, Gass P, Häberle L, Heindl F, Heusinger K, Lotz L, Lubrich H, Preuß C. Predicting mammographic density with linear ultrasound transducers. *European Journal of Medical Research*. 2023;28(1):384.

23. Wu N, Geras KJ, Shen Y, Su J, Kim SG, Kim E, Wolfson S, Moy L, Cho K, editors. Breast Density Classification with Deep Convolutional Neural Networks. 2018 IEEE International Conference on Acoustics, Speech and Signal Processing (ICASSP); 2018 2018-04-01: IEEE.

24. Ciatto S, Bernardi D, Calabrese M, Durando M, Gentilini MA, Mariscotti G, Monetti F, Moriconi E, Pesce B, Roselli A. A first evaluation of breast radiological density assessment by QUANTRA software as compared to visual classification. *The Breast*. 2012;21(4):503-6.

25. Lehman CD, Yala A, Schuster T, Dontchos B, Bahl M, Swanson K, Barzilay R. Mammographic breast density assessment using deep learning: clinical implementation. *Radiology*. 2019;290(1):52-8.

26. Yala A, Mikhael PG, Strand F, Lin G, Smith K, Wan Y-L, Lamb L, Hughes K, Lehman C, Barzilay R. Toward robust mammography-based models for breast cancer risk. *Science Translational Medicine*. 2021;13(578):eaba4373.

27. Yeoh HH, Liew A, Phan R, Strand F, Rahmat K, Nguyen TL, Hopper JL, Tan M. RADIFUSION: A multi-radiomics deep learning based breast cancer risk prediction model using sequential mammographic images with image attention and bilateral asymmetry refinement. *arXiv preprint arXiv:230400257*. 2023.

28. Pertuz S, Torres GF, Tamimi R, Kamarainen J, editors. Open framework for mammography-based breast cancer risk assessment. 2019 IEEE EMBS International Conference on Biomedical & Health Informatics (BHI); 2019: IEEE.

29. Leong L, Wolfgruber T, Quon B, Bunnell A, Valdez D, Fukui J, Hernandez B, Shvetsov Y, Kerlikowske K, Shepherd JA, editors. Image-Based Models for Predicting Advanced Breast Cancer Risk. 10th International Breast Density & Cancer Risk Assessment Workshop; 2023 06/07/2023; Kailua-Kona, HI.

30. Bunnell A, Hung K, Shepherd JA, Sadowski P. BUSClean: Open-source software for breast ultrasound image pre-processing and knowledge extraction for medical AI. *arXiv*. 2024. doi: 10.48550/arXiv.2407.11316.

31. Paszke A, Gross S, Massa F, Lerer A, Bradbury J, Chanan G, Killeen T, Lin Z, Gimelshein N, Antiga L, Desmaison A, Kopf A, Yang E, DeVito Z, Raison M, Tejani A, Chilamkurthy S, Steiner B, Fang L, Bai J, Chintala S. PyTorch: An Imperative Style, High-Performance Deep Learning Library. In: Wallach H, Larochelle H, Beygelzimer A, Alch'Y-Buc Fdt, Fox E, Garnett R, editors. 2019.

32. Huang G, Liu Z, Van Der Maaten L, Weinberger KQ, editors. Densely connected convolutional networks. Proceedings of the IEEE conference on computer vision and pattern recognition; 2017.

33. Dosovitskiy A, Beyer L, Kolesnikov A, Weissenborn D, Zhai X, Unterthiner T, Dehghani M, Minderer M, Heigold G, Gelly S. An image is worth 16x16 words: Transformers for image recognition at scale. *arXiv preprint arXiv:201011929*. 2020.

34. He K, Zhang X, Ren S, Sun J, editors. Deep residual learning for image recognition. Proceedings of the IEEE conference on computer vision and pattern recognition; 2016.

35. Akiba T, Sano S, Yanase T, Ohta T, Koyama M, editors. Optuna: A Next-generation Hyperparameter Optimization Framework. International Conference on Knowledge Discovery and Data Mining; 2019: ACM.

36. Kendall MG. A new measure of rank correlation. *Biometrika*. 1938;30(1-2):81-93.

37. Abadi M, Moore DR. Selection of circular proposals in building projects: an MCDM model for lifecycle circularity assessments using AHP. *Buildings*. 2022;12(8):1110.

38. Kokhlikyan N, Miglani V, Martin M, Wang E, Alsallakh B, Reynolds J, Melnikov A, Kliushkina N, Araya C, Yan S. Captum: A unified and generic model interpretability library for pytorch. *arXiv preprint arXiv:200907896*. 2020.

39. Qi Z, Khorram S, Li F, editors. Visualizing Deep Networks by Optimizing with Integrated Gradients. CVPR workshops; 2019.

40. Sanabria SJ, Goksel O, Martini K, Forte S, Frauenfelder T, Kubik-Huch RA, Rominger MB. Breast-density assessment with hand-held ultrasound: A novel biomarker to assess breast cancer risk and to tailor screening? *European radiology*. 2018;28:3165-75.

41. Duric N, Sak M, Fan S, Pfeiffer RM, Littrup PJ, Simon MS, Gorski DH, Ali H, Purrington KS, Brem RF. Using whole breast ultrasound tomography to improve breast cancer risk assessment: A novel risk factor based on the quantitative tissue property of sound speed. *Journal of clinical medicine*. 2020;9(2):367.

42. Glide C, Duric N, Littrup P. Novel approach to evaluating breast density utilizing ultrasound tomography. *Medical physics*. 2007;34(2):744-53.

43. O'Flynn EAM, Fromageau J, Ledger AE, Messa A, D'Aquino A, Schoemaker MJ, Schmidt M, Duric N, Swerdlow AJ, Bamber JC. Ultrasound Tomography Evaluation of Breast Density. *Investigative Radiology*. 2017;52(6):343-8. doi: 10.1097/rli.0000000000000347.

44. Fear E, Bourqui J, Mojabi P, Docktor B-J, Garland A, Deutscher D, Lasemiimeni Z, McMahon K, Besler B, Tsang R. Abstract PO3-07-08: Breast density estimation with a microwave-frequency imaging system. *Cancer Research*. 2024;84(9_Supplement):PO3-07-8-PO3--8.

45. Shepherd JA, Malkov S, Fan B, Laidevant A, Novotny R, Maskarinec G. Breast density assessment in adolescent girls using dual-energy X-ray absorptiometry: a feasibility study. *Cancer Epidemiology Biomarkers & Prevention*. 2008;17(7):1709-13.

46. Lloyd R, Pirikahu S, Walter J, Cadby G, Darcey E, Perera D, Hickey M, Saunders C, Karnowski K, Sampson DD. Alternative methods to measure breast density in younger women. *British journal of cancer*. 2023;128(9):1701-9.

47. Maskarinec G, Morimoto Y, Laguña MB, Novotny R, Guerrero RTL. Bioimpedance to assess breast density as a risk factor for breast cancer in adult women and adolescent girls. *Asian Pacific journal of cancer prevention: APJCP*. 2016;17(1):65.

48. Gutiérrez-Lopez M, Prado-Olivarez J, Matheus-Troconis C, Padilla-Medina A, Barranco-Gutiérrez AI, Espinosa-Calderon A, Herrera-Ramírez CA, Diaz-Carmona J. A Case Study in Breast Density Evaluation Using Bioimpedance Measurements. *Sensors*. 2022;22(7):2747.

49. Kaizer L, Fishell EK, Hunt JW, Foster FS, Boyd NF. Ultrasonographically defined parenchymal patterns of the breast: relationship to mammographic patterns and other risk factors for breast cancer. *The British Journal of Radiology*. 1988;61(722):118-24.

50. Hou X-Y, Niu H-Y, Huang X-L, Gao Y. Correlation of breast ultrasound classifications with breast cancer in Chinese women. *Ultrasound in Medicine & Biology*. 2016;42(11):2616-21.

51. Lee SH, Moon WK. Glandular tissue component on breast ultrasound in dense breasts: a new imaging biomarker for breast cancer risk. *Korean Journal of Radiology*. 2022;23(6):574.

52. Lee SH, Ryu H-S, Jang M-J, Yi A, Ha SM, Kim S-Y, Chang JM, Cho N, Moon WK. Glandular Tissue Component and Breast Cancer Risk in Mammographically Dense Breasts at Screening Breast US. *Radiology*. 2021;301(1):57-65. doi: 10.1148/radiol.2021210367.

53. Kim WH, Lee SH, Chang JM, Cho N, Moon WK. Background echotexture classification in breast ultrasound: inter-observer agreement study. *Acta Radiologica*. 2017;58(12):1427-33.

54. Chang RF, Hou YL, Lo CM, Huang CS, Chen JH, Kim WH, Chang JM, Bae MS, Moon WK. Quantitative analysis of breast echotexture patterns in automated breast ultrasound images. *Medical physics*. 2015;42(8):4566-78.

55. Wang AT, Vachon CM, Brandt KR, Ghosh K, editors. *Breast density and breast cancer risk: a practical review*. Mayo Clinic Proceedings; 2014: Elsevier.

56. Zhu X, Wolfgruber TK, Leong L, Jensen M, Scott C, Winham S, Sadowski P, Vachon C, Kerlikowske K, Shepherd JA. Deep Learning Predicts Interval and Screening-detected Cancer from Screening

Mammograms: A Case-Case-Control Study in 6369 Women. *Radiology*. 2021;301(3):550-8. doi: 10.1148/radiol.2021203758. PubMed PMID: 34491131.

57. State of Hawaii Department of Business Economic Development and Tourism. Annual Estimates of the Resident Population by Sex, Race, and Hispanic Origin for Hawaii: April 1, 2020 to July 1, 2023 (SC-EST2023-SR11H-15). June 2024.

58. Maskarinec G, Meng L, Ursin G. Ethnic differences in mammographic densities. *International journal of epidemiology*. 2001;30(5):959-65. doi: 10.1093/ije/30.5.959.

59. Habel LA, Capra AM, Oestreicher N, Greendale GA, Cauley JA, Bromberger J, Crandall CJ, Gold EB, Modugno F, Salane M, Quesenberry C, Sternfeld B. Mammographic density in a multiethnic cohort. *Menopause (New York, NY)*. 2007;14(5):891-9. doi: 10.1097/gme.0b013e318032569c.

FIGURE LEGENDS

TABLES

SUPPLEMENTAL MATERIALS

Supplement

HIPIMR description: The HIPIMR collects data from three clinical partners: Clinic 1 is a nonprofit healthcare network (comprising four medical centers); Clinic 2 is a private nonprofit tertiary hospital; and Clinic 3 is a diagnostic medical imaging center from 2009-2023 on the island of O‘ahu. The HIPIMR is matched to the Hawai‘i Tumor Registry for retrieval of biopsy- or surgery-confirmed cancer labels. All included mammograms were taken on Hologic Selenia (65.0%) or Selenia Dimensions (35.0%) machines. 89.7% of included BUS images were captured on a Philips Medical Systems IU22 system.

Inclusion/exclusion criteria: Women were selected for inclusion if they: (a) had at least one negative screening 2D mammography visit; (b) had a negative, benign, or probably benign (BI-RADS 1, 2, or 3) BUS visit within one year of the recorded screening mammography visit; (c) had a clinical BI-RADS breast density recorded at their screening mammogram; (d) had the standard four views (left craniocaudal, right craniocaudal, left mediolateral oblique, and right mediolateral oblique) captured at their screening mammogram; and (e) had no history of breast cancer prior to screening mammogram. Women with missing mammographic density categories, BI-RADS scores, or imaging were excluded. Male patients were also excluded. Missing covariate data were not imputed but reported as missing. Case-control matching was performed on the testing set only.

Curated and uncurated validation sets: The curated validation and testing sets had the complete preprocessing pipeline applied, while the training and uncurated validation sets had only invalid scans removed and dual-view scans split. Training performance was monitored on both the curated and uncurated validation sets as an indicator for the presence of model dependence on spurious correlations with scan artifacts.

Deep learning architecture modifications: To conform with model architectures developed on three-channel RGB images, scans are cropped to 224 by 224 pixels (images measuring less than 224 pixels on either dimension have their smaller edge resized to 224 prior to cropping), per-image min-max normalized, and fed through a single convolutional layer with a 1-by-1 kernel and three filters before being passed to an ImageNet-pretrained architecture (4). The final fully-connected layer of the architecture is augmented with random dropout.

Table 1. Hyperparameter search space for all Optuna trials for all deep learning architectures tested. DenseNet121 was selected based on clean validation performance. Architecture weights were 25 trials using the TPESampler in Optuna (2).

Architecture	Chosen Value					Dirty Validation AUC [‡]	Clean Validation AUC [‡]
	Learning Rate [1e-7, 1e-3] [*]	Batch Size {64, 128, 256, 512}	Apply ColorJitter in Training {True, False}	First Trainable Backbone Unit {0, 1, 2, 3, 4} [†]	Penultimate Dropout Proportion [0.0, 0.1, ..., 0.9]		
ResNet50	1.19e-7	512	False	0	0.9	0.861	0.805
DenseNet121	5.28e-7	256	False	4	0.9	0.864	0.840
ViTB32	5.46e-7	64	True	1	0.3	0.849	0.833

*Learning rate was sampled from a logarithmic uniform distribution. All other variables are sampled from a categorical distribution.

[†]Integer values correspond to the first “unit” of the backbone architecture which was unfrozen for training, with 0 meaning the entire backbone is trainable. We define the choices 1, 2, 3, and 4 for each of the backbones as follows: ResNet50 Layers 1, 2, 3, and 4; DenseNet121 Dense Blocks 1, 2, 3, and 4; ViTB32 Encoder Layers 3, 6, 9, and 12.

[‡]Micro-averaged AUC over all density categories.

Training configuration details: Training was done with the Adam optimizer (5) and the learning rate degraded by half when no improvement in training loss is seen for 10 epochs. Training is stopped when no improvement in validation loss is observed for 25 epochs. During training, images were augmented with random cropping, rotation, and brightness/contrast jitter. In testing, images were center-cropped.

Jud method implementation details: Jud et. al collect experimental breast ultrasound and mammography images for 93 prospectively-recruited patients. As their images were not collected clinically, there are no imaging artifacts present. Thus, our *curated* validation set most closely reflects the development and testing environment of Jud et. al. 16-bin gray-level image histograms were calculated according to Jud et al's definition, evenly-spaced based on grayscale pixel value: [0, 15], [16, 31], etc. (3). We compared performance with and without per-image min-max normalization of gray-levels prior to binning. Models were optimized over five-fold cross-validation (by woman) on the curated validation set via grid search (see **Supplemental Table 2**). Predictions were arithmetically averaged for each woman to generate a final breast density prediction. Final linear (logistic regression) and non-linear (MLP or random forest) models were chosen based on performance on the curated validation set

Statistical analysis step 1: Micro-averaging of the AUROC measures how well the AI model predicts breast density when performance is weighted equivalently for all ground-truth breast density categories. Micro-averaging weights all instances equally in metric computation, creating a global metric natively. Macro-averaging calculates class-wise metrics, then takes a global average. Subgroup performance by micro-averaged AUROC is established solely on the testing set. 95% confidence intervals for AUROC are estimated using DeLong's method (6, 7). All subgroups are defined by metadata collected at time-of-exam or by cancer status collected from the Hawai'i Tumor Registry.

Statistical analysis step 2: Logistic regression models were constructed using 3-fold cross-validation, split by woman, on the case-control matched testing set. Logistic regression models were constructed and compared for two different measures of mammographic breast density: clinical BI-RADS breast density and BI-RADS breast density predicted by the best-performing AI model (DenseNet121). For each woman, 100 data points were simulated by independent random sampling from the predicted breast density distribution. A logistic regression was fit on all 107,400 simulated points. For odds ratio estimation, a single density was randomly sampled from the predicted distribution for each woman.

Table 2. Hyperparameter search space for all machine learning (ML) methods from the 16 gray-level bins defined in (3). Hyperparameters were chosen based on 5-fold cross validation on the clean validation set.

ML Models	Chosen Value		Clean Validation AUC [‡]
	Selected Hyperparameters	Normalization	
Logistic Regression	C: 10 Regularization method: L1 Solver: Saga	Yes	0.638
MLP	Activation: ReLU Learning rate: 0.0001 Hidden layer size: 512 Optimizer: Adam LR Schedule: Constant	Yes	0.741
Random Forest	Max tree depth: None Min samples per leaf: 1 Min samples per split: 2 Number of trees: 200	No	0.965

[‡]Micro-averaged AUC over all density categories.

Inclusion/exclusion criteria-specific counts. 108 and 1,441 women were excluded from the testing and development sets, respectively, due to all US images being captured as part of a biopsy procedure. Of the 14,083 women remaining, 17 women were excluded due to exclusion of all their BUS images being invalid. 459,161 images were retrieved from all included women. After exclusion of images captured as part of a biopsy procedure (n = 51,049) and invalid images (n = 4,119) and splitting dual-view images (n = 1,715), 407,423 images remained. After removal of elastography and Color Doppler scans from the testing set, 405,120 total BUS images remained.

Table 3. Odds ratios for cancer risk logistic regression models presented in the main text. Geras Density refers to density values obtained from the classifier presented in (1).

	Odds Ratio (95% CI)		
	Clinical Density	BUS Density	Geras Density
Fatty/A	1.24 (0.87, 1.77)	1.07 (0.74, 1.55)	1.15 (0.80, 1.64)
Scattered/B	1.00 (Reference)	1.00 (Reference)	1.00 (Reference)
Heterogeneous/C	1.11 (0.63, 1.97)	1.11 (0.66, 1.86)	1.19 (0.70, 2.04)
Dense/D	1.54 (1.31, 1.81)	1.50 (1.28, 1.76)	1.51 (1.29, 1.77)
Age*	0.56 (0.19, 1.65)	1.12 (0.31, 4.09)	0.96 (0.40, 2.30)

*Age is standardized to unit variance and zero mean.

Table 4. Subgroup performance statistics for the DenseNet121, logistic regression, and random forest models.

	DenseNet121		Logistic Reg		Random Forest	
	Per-Image	Per-Patient	Per-Image	Per-Patient	Per-Image	Per-Patient
AUC* (95% C.I.)	0.840 (0.838, 0.842)	0.854 (0.842, 0.866)	0.771 (0.768, 0.774)	0.795 (0.781, 0.809)	0.759 (0.756, 0.762)	0.794 (0.780, 0.808)
by US machine manufacturer	PHILIPS	0.838 (0.836, 0.841)	0.853 (0.839, 0.866)	0.766 (0.763, 0.770)	0.789 (0.773, 0.806)	0.761 (0.758, 0.764)
	ATL	0.870 (0.863, 0.876)	0.864 (0.829, 0.900)	0.809 (0.801, 0.817)	0.831 (0.789, 0.872)	0.749 (0.740, 0.758)
	TOSHIBA [‡]	0.883 (0.862, 0.905)	0.912 (0.870, 0.954)	0.814 (0.788, 0.841)	0.856 (0.809, 0.903)	0.778 (0.750, 0.805)
	SIEMENS [‡]	0.718 (0.692, 0.744)	0.793 (0.731, 0.855)	0.699 (0.672, 0.727)	0.739 (0.668, 0.811)	0.687 (0.659, 0.715)
by binned age (years) at US exam	< 50	0.855 (0.852, 0.858)	0.875 (0.859, 0.891)	0.754 (0.749, 0.758)	0.792 (0.772, 0.814)	0.744 (0.740, 0.749)
	[50, 65)	0.825 (0.821, 0.829)	0.843 (0.823, 0.863)	0.775 (0.770, 0.779)	0.795 (0.772, 0.818)	0.765 (0.761, 0.770)
	≥ 65	0.826 (0.820, 0.833)	0.818 (0.786, 0.851)	0.809 (0.802, 0.816)	0.793 (0.757, 0.829)	0.787 (0.780, 0.794)
by cancer status	Benign	0.844 (0.841, 0.846)	0.854 (0.841, 0.867)	0.769 (0.767, 0.772)	0.793 (0.778, 0.809)	0.759 (0.756, 0.762)
	Malignant	0.822 (0.816, 0.828)	0.853 (0.825, 0.882)	0.780 (0.773, 0.787)	0.803 (0.769, 0.837)	0.758 (0.751, 0.766)
by US exam BI-RADS category	BI-RADS 1	0.826 (0.819, 0.833)	0.858 (0.829, 0.887)	0.785 (0.777, 0.792)	0.812 (0.779, 0.845)	0.767 (0.760, 0.775)
	BI-RADS 2	0.831 (0.828, 0.834)	0.841 (0.825, 0.858)	0.752 (0.748, 0.756)	0.777 (0.758, 0.797)	0.740 (0.736, 0.744)
	BI-RADS 3	0.868 (0.864, 0.873)	0.879 (0.859, 0.900)	0.808 (0.803, 0.814)	0.820 (0.794, 0.846)	0.799 (0.793, 0.804)

*AUC is a micro-averaged one vs. rest AUROC over all density categories, except for density subgroups. For density subgroups, one vs. rest AUC for each category is shown. 95% confidence intervals are calculated using DeLong's method (1, 2).

[‡]Denotes subgroups for which there are fewer than 100 unique women.

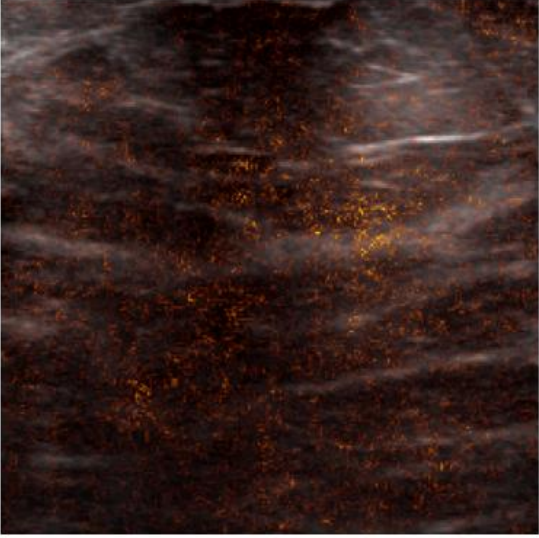
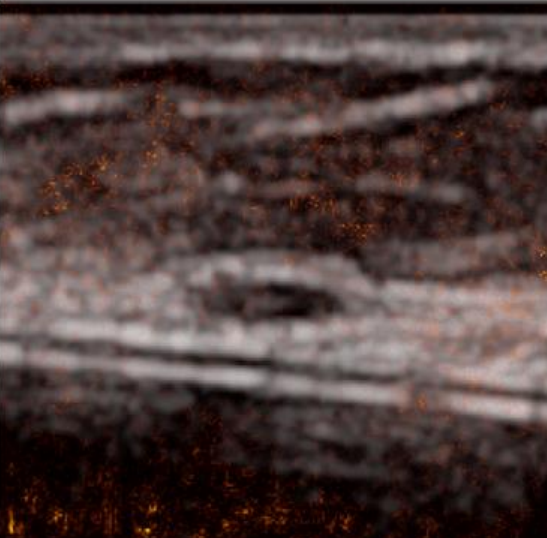
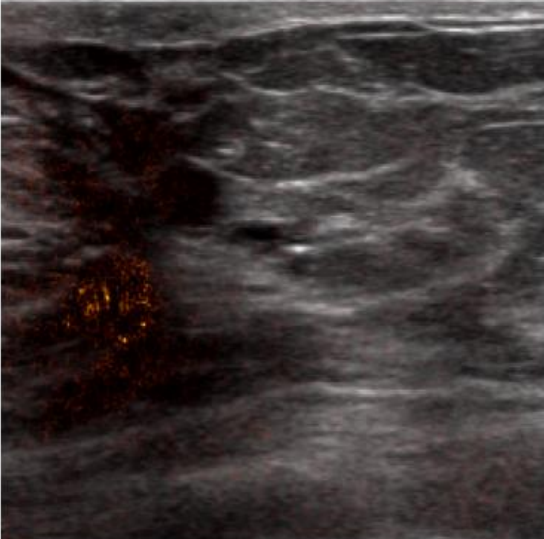
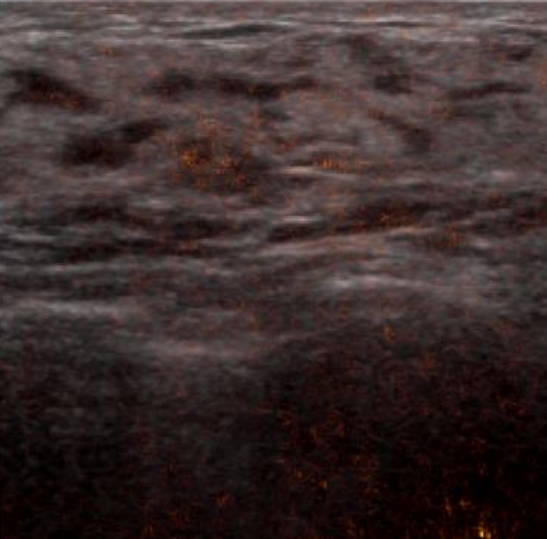
		Predicted Classification	
		A/B	C/D
True Classification	A/B		
		P(B) = 0.560 True density A	P(D) = 0.727 True density B
C/D	C/D		
		P(B) = 0.482 True density D	P(D) = 0.661 True density D

Figure 1 Confusion matrix style visualization of integrated gradient maps for model predictions. All images are from the unseen test set.

REFERENCES

1. Wu N, Geras KJ, Shen Y, Su J, Kim GS, Kim E, Wolfson S, Moy L, Cho K. Breast density classification with deep convolutional neural networks. ICASSP. 2018. doi: <https://doi.org/10.48550/arXiv.1711.03674>.

2. Akiba T, Sano S, Yanase T, Ohta T, Koyama M, editors. Optuna: A Next-generation Hyperparameter Optimization Framework. International Conference on Knowledge Discovery and Data Mining; 2019: ACM.
3. Jud SM, Häberle L, Fasching PA, Heusinger K, Hack C, Faschingbauer F, Uder M, Wittenberg T, Wagner F, Meier-Meitinger M, Schulz-Wendtland R, Beckmann MW, Adamietz BR. Correlates of mammographic density in B-mode ultrasound and real time elastography. European Journal of Cancer Prevention. 2012;21(4):343-9.
4. Deng J, Dong W, Socher R, Li LJ, Kai L, Li F-F, editors. ImageNet: A large-scale hierarchical image database. 2009 IEEE Conference on Computer Vision and Pattern Recognition; 2009 20-25 June 2009.
5. Kingma DP, Ba J. Adam: A method for stochastic optimization. arXiv preprint arXiv:14126980. 2014.
6. Jacob G. A python library for confidence intervals. 2023.
7. Sun X, Xu W. Fast implementation of DeLong's algorithm for comparing the areas under correlated receiver operating characteristic curves. IEEE Signal Processing Letters. 2014;21(11):1389-93.